

Clustered bottlenecks in mRNA translation and protein synthesis

Tom Chou¹ and Greg Lakatos²

¹Dept. of Biomathematics and IPAM, UCLA, Los Angeles, CA 90095

²Dept. of Physics, University of British Columbia, Vancouver, BC Canada V6T 1Z2

October 29, 2018

Abstract

We construct an algorithm that generates large, band-diagonal transition matrices for a totally asymmetric exclusion process (TASEP) with local hopping rate inhomogeneities. The matrices are diagonalized numerically to find steady-state currents of TASEPs with local variations in hopping rate. The results are then used to investigate clustering of slow codons along mRNA. Ribosome density profiles near neighboring clusters of slow codons interact, enhancing suppression of ribosome throughput when such bottlenecks are closely spaced. Increasing the slow codon cluster size, beyond $\approx 3 - 4$, does not significantly reduce ribosome current. Our results are verified by extensive Monte-Carlo simulations and provide a biologically-motivated explanation for the experimentally-observed clustering of low-usage codons.

05.10.-a, 87.16.Ac, 87.10.+e

During protein synthesis, ribosome molecules initiate at the 5' end of messenger RNA (mRNA), scan (“elongate”) along the mRNA sequence, and terminate with the completed protein product at the 3' termination end (Fig. 1a). Each elongation step requires reading (translating) a nucleotide triplet (codon) and the binding of a freely diffusing transfer RNA (tRNA) molecule carrying the amino acid specific to each codon [1]. Besides being a critical final stage of gene expression *in vivo*, control of protein synthesis is vital protein adaptation and evolution [2, 3, 4], in control of viral parasitism [5], and in the biotechnology of high yield, cell-free, synthetic *in vitro* protein production [6, 7].

The near-final stage of protein expression can be regulated by exploiting local variations in ribosome detachment and elongation rates (arising from different codon usages for any given amino acid). Relative concentrations of tRNA in solution can be a factor in determining local ribosome translation rates. This fact has been exploited in the modification of green fluorescent protein codons to match those preferred in mammalian systems, thereby optimizing expression levels [8]. Binding of an incorrect tRNA can also temporarily prevent binding of the correct tRNA for a particular codon, slowing down elongation [1]. Regions of higher ribosome density can also protect the substrate mRNA from the action of enzymes which arrest translation. Finally, local pauses may provide time for regions of the peptide to sequentially fold before the integration of additional amino acids.

The occurrence of “slow” codons (those with rare corresponding tRNA and/or amino acids), along mRNA is known to inhibit protein production [9, 10], and is conjectured to serve a regulatory role in protein synthesis. Such “bottleneck” or “defect” codons (and the amino acids for which they code) arise infrequently, and typically include CTA (Leu), ATA (Ile), ACA (Thr), CCT and CCC (Pro), CGG, AGA, and AGG (Arg) [11, 12]. Statistics indicate a higher occurrence of rare codons

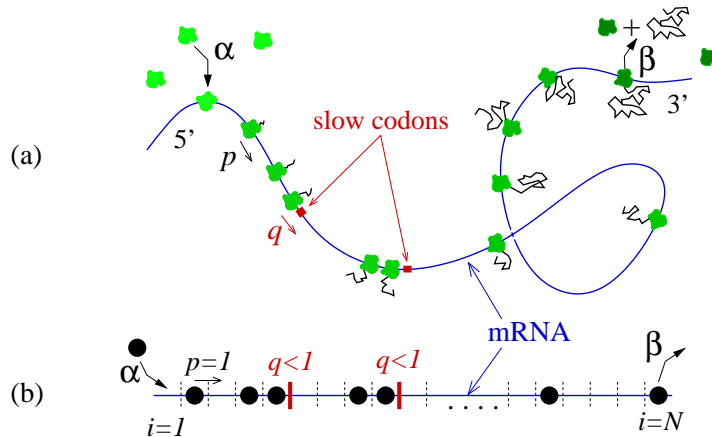


Figure 1: (a) The mRNA translation/protein synthesis process. Multiple ribosomes (polysomes) move unidirectionally along mRNA as tRNA (not shown) deliver the appropriate amino acid to the growing chain. Codons with low concentrations of corresponding tRNA result in bottlenecks that locally suppress ribosome motion across it. (b) A simple totally asymmetric exclusion process on N lattice sites used to model mRNA translation in the presence of slow codons bottlenecks, or “defects.”

near the 5' initiation site of *E. coli* genes [13]. Even more striking is the bias for rare codons to cluster [11]. Statistical analyses show small (2-5) clusters of rare codons occur frequently in *E. coli*, *Drosophila*, yeast, and primates [11, 14].

Although the strength, number, and positioning of bottlenecks along an mRNA chain undergoing translation clearly affect local ribosome densities and overall translation rates, there has been no quantitative model describing how various bottleneck motifs control ribosome throughput and protein synthesis. In this paper, we consider a simple physical model of how specific codon usages that give rise to local delays in elongation can be used to suppress protein synthesis. Our results provide biophysical hypotheses for slow codon clustering within a simple nonequilibrium steady-state stochastic framework. Ribosome density boundary layers surrounding two nearby bottlenecks, or defects are shown to act synergistically to regulate and amplify the suppression of protein production.

We model mRNA translation by ribosome particles using a nonequilibrium totally asymmetric exclusion process (TASEP) [15, 16] with a few carefully distributed slow sites (cf. Fig. 1b). In the TASEP, ribosome particles attach (initiate) at the first lattice site with rate α , only if the first site is empty. Interior ribosome particles can move forward with rate p_i from site i to site $i + 1$ only if site $i + 1$ is empty. For each step a ribosome moves forward, a codon is read, and an amino acid-carrying tRNA delivers its amino acid to the growing polypeptide chain. No motion is allowed if the site in front of a particular ribosome is occupied. Each ribosome that reaches the last site $i = N$ (the 3' termination site) has polymerized a complete protein and detaches with rate β .

In the case of *uniform* $p_i = 1$, the protein production rate (*e.g.* the steady-state ribosome current) and ribosome density along the mRNA are known exactly in terms of α and β [15, 16]. In the long chain ($N \rightarrow \infty$) limit, the steady-state results reduce to simple forms illustrating the fundamental physical regimes. The current may be entry-rate limited ($\alpha < 1/2, \alpha < \beta$), where the ribosome density is low and the steady-state current $J(\alpha) = \alpha(1 - \alpha)$ depends only on α . If β is sufficiently small ($\beta < 1/2, \beta < \alpha$), the density is high and the current $J(\beta) = \beta(1 - \beta)$ is a function of the rate-limiting exit step only. When both $\alpha, \beta > 1/2$, the rate-limiting processes are

the uniform internal hopping rates, and the steady-state current reaches its maximum attainable value $J = 1/4$. These three regimes define a phase diagram or the steady-state current of the TASEP. For a typical mRNA length of $\sim 100 - 1000$ codons, these simple analytic forms for J are extremely accurate. For the analyses in the absence of ribosome detachments, we shall restrict our attention to effectively the $N \rightarrow \infty$ limit.

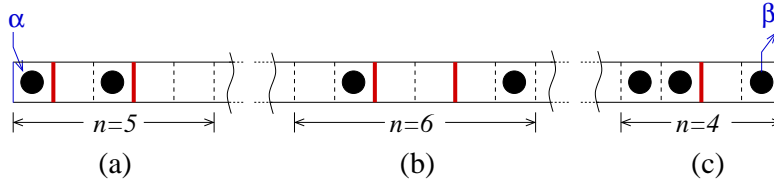


Figure 2: Placements of slow defects, or rare-usage codons (thick red segments). (a) Two defects near the initiation site straddled by an $n = 5$ lattice segment. (b) Two defects in the chain interior, away from the boundaries, $n = 6$. (c) A single slow defect near the termination end of the chain, $n = 4$.

There is no general theory for computing steady-state particle (ribosome) currents when the internal hopping rates p_i vary arbitrarily with lattice position i . However, specific motifs $\{p_i\}$ (such as isolated defects [17] and periodic variations) can be treated with approximations and simulation. Since slow codons are also rare, with typical densities of 0.03, we will consider simple configurations of few, identical bottlenecks (with hopping rate $q < 1$) distributed within an otherwise uniform (with rate 1) lattice. Finite numbers of “fast” defects with $q > 1$ do not affect steady-state currents since the rate limiting hops $p_i = 1$ dominate the lattice. Figures 2(a-c) show hypothetical placements of defects near the 5’ initiation end, the mRNA interior, and the 3’ termination end. Within a finite segment (of length $n = 5, 6, 4$ sites in Figs. 2, respectively) straddling the bottlenecks, we explicitly enumerate all 2^n distinct states according to the algorithm indicated in Fig. 3. This generates a *band-diagonal* (of width n) $2^n \times 2^n$ matrix coupling the probabilities P_j , ($1 \leq j \leq 2^n$) that the segment is in state j .

Now consider an interior segment (Fig. 2(b)). The mean density in the site immediately to the left(right) of the segment is denoted $\sigma_- (\sigma_+)$. The transition matrix contains the parameters σ_{\pm} since entry and exit into the enumerated segment is proportional to σ_- and $1 - \sigma_+$, respectively. The steady-state current is calculated from the appropriate elements of the singular eigenvector associated with the zero-eigenvalue of the transition matrix. For example, the particle flux out of the rightmost site of the segment is $J(\sigma_-, \sigma_+, \{p_i\}) = (1 - \sigma_+) \sum_{j=\text{odd}} P_j(\sigma_-, \sigma_+, \{p_i\})$, since the odd states correspond to those with a particle at the last site in the segment. The singular eigenvector of the $2^n \times 2^n$, sparse, band-diagonal transition matrix was computed (up to $n \approx 18$) using an implicit restarted Arnoldi iteration method [18] found in Matlab. The effects of the perturbed particle correlations surrounding a bottleneck are accounted for provided n is larger than the density boundary layer thickness. Since the densities are uniform far enough away from the defects, we assume that they are also $\sigma_- (\sigma_+)$ far to the left(right) of the segment. Thus, the mean-field currents well to the left and right of the segment are $J_- = \sigma_- (1 - \sigma_-) = J_+ = \sigma_+ (1 - \sigma_+)$. The only physical solution is $\sigma_- = 1 - \sigma_+$. Equating $J(\sigma_- = 1 - \sigma_+, \sigma_+, \{p_i\}) = \sigma_+ (1 - \sigma_+)$, and solving for σ_+ numerically, we find the ribosome current J . For $\alpha < 1/2$ and defects near the initiation end, we simply equate $J(\alpha, \sigma_+, \{p_i\}) = \sigma_+ (1 - \sigma_+)$ and solve for σ_+ . For $\beta < 1/2$ and defects near the termination end, σ_- is determined from $\sigma_- (1 - \sigma_-) = J(\sigma_-, \beta, \{p_i\})$. We used this improved, systematic finite-segment mean-field theory (FSMFT) to compute currents of TASEPs

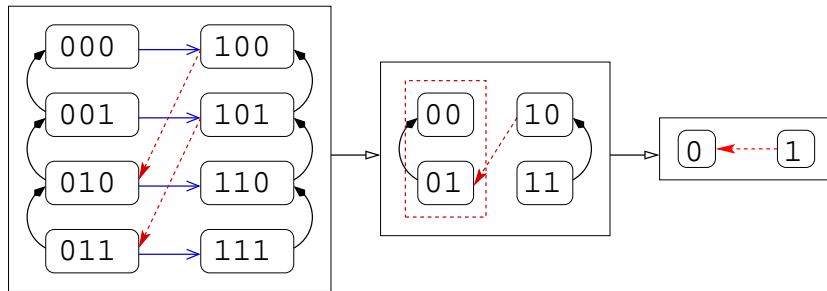


Figure 3: The algorithm that generates the transition matrix for a TASEP. For illustration, consider a three site model. Each possible occupancy of the lattice is associated with a bit pattern, and the state is enumerated with the corresponding decimal value. For example given that 011 is the binary representation of 3, we label the state with particles occupying the second and third lattice sites as *state 3*. Next we divide the states into two groups; states where the first lattice site is occupied (*1-states*), and states where the first lattice site is empty (*0-states*). Regardless of the number of lattice sites in the TASEP, the transitions between the two classes of states *always* occur between the first half of the *1-states* and the second half of the *0-states* (dashed red arrows). To determine the remaining transitions we call the algorithm recursively on both the *1-states* and the *0-states*, making sure to ignore the highest order bit (*i.e.* the leftmost lattice site). Finally we add in the trivial transitions between each *0-state* and each *1-state* that are the result of injection at the left edge of the lattice (blue arrows). With the connectivity of the states fully enumerated, assigning the appropriate rate p_i to each of the transitions is straightforward.

with representative placements of internal defects. In practice, segment lengths that include only 2-3 sites on each side of a defect were sufficient for obtaining extremely accurate results. Efficient continuous-time Monte-Carlo simulations using the Bortz-Kalos-Lebowitz (BKL) algorithm [19, 20] were performed on lattices of size $N \geq 10000$ to verify and extend all our results.

MC simulations show that for $\alpha, \beta > 1/2$, the currents J are insensitive to the position of defects. The behavior for $\alpha, \beta < 1/2$ resembles an interior defect near the initiation or termination end. Slow initiation and/or termination rates can be effectively described by defects ($q < 1$) near the ends of the lattice. Therefore, we can restrict our analysis to large $\alpha, \beta \gg 1/2$. Hopping across a single interior defect (with rate $q < 1$) is the overall rate-limiting step. For this single defect, the reduced steady-state current $J_1(q)$, found from both FSMFT and MC simulations are shown in Fig. 4(a). The $n = 4$ FSMFT yields currents within 2% of those computed from MC simulations. The least-accurate $n = 0$ FSMFT gives $J = q/(q + 1)^2$ and is equivalent to previous treatments of a single defect [17]. Larger segments n yield increasingly unwieldy algebraic expression for $J_1(q)$. The FSMFT (which is exact if $n = N$) is asymptotically correct for $q \rightarrow (0, 1)$ and is a systematic expansion in $J = \sum_{i=1}^{\infty} a_i q^i$ about $q = 0$. Coefficients up a_{n+1} can be shown to be given correctly by a $2n$ -segment MFT, *i.e.*, for $n \geq 1$, $J \sim q - 3q^2/2 + \mathcal{O}(q^3)$ rather than $J \sim q - 2q^2 + \mathcal{O}(q^3)$ predicted by the 0-segment MFT [17].

The current J can be further reduced upon adding successive, contiguous defects. The steady-state current across m equivalent, contiguous interior bottlenecks can be shown to have the analytic expansion

$$J_m(q \rightarrow 0) \sim \left(\frac{m+1}{4m-2} \right) q + \mathcal{O}(q^2). \quad (1)$$

As m increases, the current is determined by the rate-limiting segment which resembles a uniform

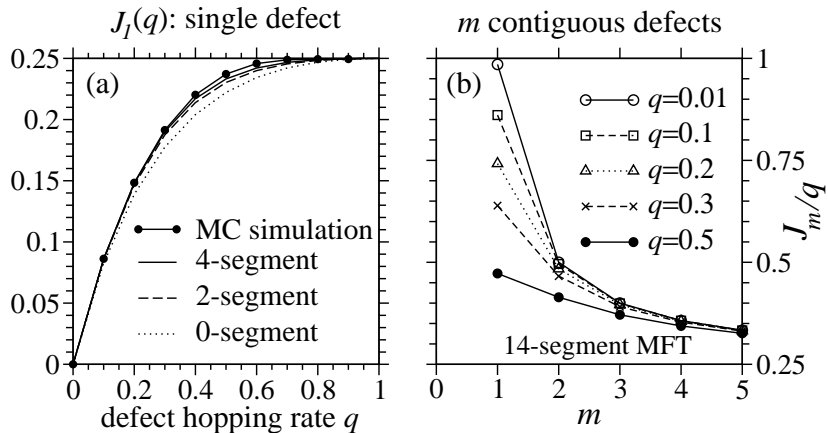


Figure 4: (a) Comparison of steady-state currents $J_1(q)$ for a single defect derived from MC simulations with those obtained from n -segment MFT. For $n \geq 4$, the FSMFT results are within 2% of those from MC simulations. The boundary injection/extraction rates were not rate limiting ($\alpha = \beta = 10$). (b) Further reduction of steady-state current as successive, identical defects are added. The first few defects cause most of the reduction in current.

chain of hopping rates q with relatively fast injection from, and extraction into, the remainder of the chain with hopping rates $p_i = 1$. Thus, the current approaches that of a long, uniform chain with hopping rates q in the maximal current regime: $J = q/4$. Figure 4(b) plots $J_m(q)/q$ for various q as a function of m defects. A 14-segment MFT was used in to generate the results and was checked to provide high numerical accuracy up to $m \approx 12$. For all $q < 1$, $J_m(q)/q$ approaches $1/4$ as $m \rightarrow N$, with the largest changes occurring for small m and q . The leading order approximation in (1) is very accurate (compared to FSMFT or MC simulations) for q as large as 0.1.

For strong bottlenecks with $q \lesssim 0.3$, the largest reduction in $J_m(q)$ occurs as $m = 1 \rightarrow 2$. Therefore, one may consider the effects of placing only two bottlenecks in the mRNA interior. Fig. 5(a) shows the expected currents $J_2(q; k)$ across a chain containing two defects spaced k sites apart. Results for $k \leq 10$ were computed using an $n = 14$ FSMFT, while those for $k > 10$ were obtained from MC simulations. The largest reduction in the current occurs when two defects are spaced as closely as possible. The current $J_2(q; k \rightarrow \infty) \rightarrow J_1(q)$ eventually approaches that for a *single* defect. A finite number of multiple defects, if spaced far apart, will not significantly decrease J relative to the case of a single defect. As k increases, the density downstream of the first defect recovers to the bulk value σ_- before encountering the second defect. This behavior is clearly shown (using both FSMFT and MC simulations) in Fig. 5(b) for a pair of defects ($q = 0.15$). For two identical defects with small q we find

$$J_2(q; k) \sim \left(\frac{k}{k+1} \right) q + \mathcal{O}(q^2). \quad (2)$$

Therefore, the current for two identical bottlenecks is at most a factor of 2 smaller than that for a single defect. This maximal contrast occurs when $q \rightarrow 0$ and when the two bottlenecks are adjacent to each other. Fig. 5(c) plots the variation in $J_2(q; k)/J_1(q)$ as a function of k for various q .

Typically, a cell has a fixed number of rare codons with which to implement different translation regulation strategies. From the two-defect current J_2 , we estimate the expected current for m *randomly* distributed bottlenecks. The current will be reduced to a value less than or equal to $J_2(q; k)$ only when two or more defects are spaced within k sites. The total number of ways m

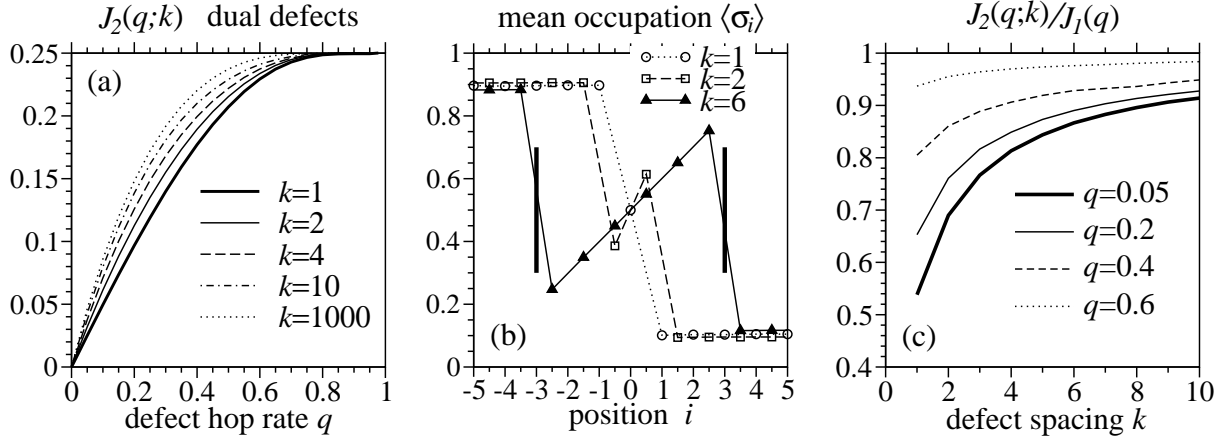


Figure 5: (a) Steady-state currents across a chain with two identical defects in the interior spaces by k lattice sites. The current is suppressed most when the defects are closely spaced. (b) The density profiles centered at the midpoint between two defects ($q = 0.15$) of various spacings k . The thick vertical bars denote the defect positions for $k = 6$. For larger k , density boundary layers heal, allowing particle build-up behind the second barrier, enhancing the current. (c) The dependence of the normalized steady-state current $J_2(q;k)/J_1(q)$ as a function of the defect separation.

defects can be placed on $N - 1$ interior sites, such that the minimum pair spacing is k is equivalent to the “Tonk’s gas” partition function for m particles of integer length k distributed on a lattice with $N - 1 + k$ sites [21]:

$$Z_k(m, N) = \binom{N - 1 - (m - 1)(k - 1)}{m}. \quad (3)$$

The probability density that the minimum inter-defect spacing equals k is thus

$$Q_k(m, N) = \frac{(Z_k(m, N) - Z_{k+1}(m, N))}{Z_1(m, N)}. \quad (4)$$

The probability density $Q_k(m, 300)$ is shown in Fig. 6(a) for $m = 4, 8, 12, 16$. For small number of defects m , the probability density is broad in k , indicating the large number of separations k uniformly accessible to any of the few pairs. As m increases, the likelihood of any pair being close increases, pushing $Q_k(m, N)$ to peak at small k .

The maximum current for any configuration with a minimum defect spacing k is $J_2(q; k)$. Thus, an upper bound for the randomness-averaged current is

$$\langle J \rangle_{ran} \leq \sum_{k=1}^{\text{int}\{(N-1)/(m-1)\}} Q_k(m, N) J_2(q; k). \quad (5)$$

This result will be very accurate if the defect density is low enough that one can neglect the probability that more than two defects each separated by k sites form a single cluster, particularly for small k . Although the most likely minimum defect spacing is $k = 1$, at low defect densities, the total probability of closely-spaced defects remains small and the weight of $Q_k(m, N)$ at larger k dominate the statistics of $\langle J \rangle_{ran}$. The disorder-averaged current $\langle J(m, N = 300) \rangle_{ran}$ (normalized by $J_1(q)$) is shown in Fig. 6(b). For very small m , the current is approximately that of a single defect. The current is most sensitive to the number of random defects at $m \approx 10$, corresponding

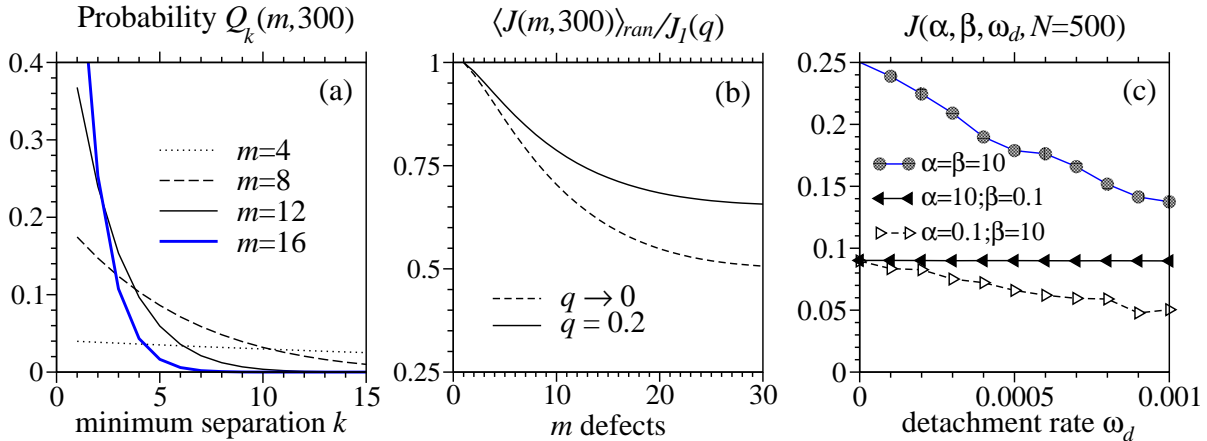


Figure 6: (a) The probability $Q_k(m, N)$ that the minimum separation of any two defects (of a total of m on an N site lattice section) is k (Eqn. (4)). (b) The upper bound for the mean current of a lattice with m defects randomly distributed within the central $N = 300$ sites (Eqn. (5)). This $J_1(q)$ -normalized, randomness-averaged upper bound includes suppression only from pairwise defect configurations. A lower bound as $m \rightarrow N - 1$ is $\langle J(m \rightarrow N - 1) \rangle_{ran} \rightarrow q/4$. (c). The effects of a small, uniform detachment rate ω_d at each site. Detachments suppress ribosome throughput only in the entry-limited ($\alpha = 0.1, \beta = 10$) and maximal current ($\alpha = \beta = 10$) regimes.

to $m/N \approx 0.03$, approximately the fraction of slow codons observed *in vivo*. Nonetheless, the observation of enhanced, nonrandom clustering suggests that other biological regulation pathways exist and would yield currents measurably below the upper bound in (5). As $m \rightarrow N - 1$, large clusters of defects dominate that are not accounted for in $Q_k(m, N)$, and the current approaches $q/4$.

Finally, we consider the effects of a small uniform ribosome detachment at each site with rate ω_d . Monte-Carlo simulations show in Fig. 6(c) that the steady-state current is diminished only when the TASEP is in what normally would be the entry-limited (small α , large β) and maximal current (large α, β) regimes. When translation is initiation-limited, detachments occur for particles that have already passed the rate-limiting initiation stage, so they no longer contribute to the final current. In the maximal current regime, interior particles are also detaching, thus reducing the number of particles that contribute to the current. In the exit-limited regime (large α , small β), detachments also decrease the overall ribosome density along most of the mRNA. However, if ω_d is small (as in Fig. 6(c)), termination remains the rate-limiting step, ribosomes are still able to pile up against the termination site, and the final ribosome throughput $J = \beta\sigma_N$ remains relatively unchanged. In the termination rate-limited regime, although the final current is not significantly suppressed by small ω_d , the high ribosomal density along the mRNA results in a large current *off* the mRNA and may be metabolically wasteful.

We have found that not only can a single defect directly inhibit elongation across it, but a few bottlenecks, properly distributed, can further slow protein production by a factor of $\sim 2 - 4$.¹ Depending on the targeted biological outcome, qualitatively distinct strategies can be employed.

¹Ribosomes are structurally larger than nucleotide triplets, occluding $w \sim 10$ codons. Although our FSMFT algorithm cannot be easily adapted for large particles, the steady-state properties of a $w > 1$ TASEP [20, 16] are qualitatively the same as the standard TASEP were each particle occupies exactly one lattice site, as verified by extensive MC simulations. However, the finite ribosome size prevents defects spaced $k \lesssim w$ codons apart to influence each other.

Although maximal current reduction is achieved by clustering defects as tightly as possible, successive addition beyond a handful of defects does little to reduce the current. Defects which are all spaced more than a handful of sites apart will not reduce the throughput more than a *single* defect. These results are qualitatively consistent with a single, localized region providing the rate limiting step(s) for translation. Since initiation, which requires assembly of numerous ribosome parts, is typically rate limiting, the observation of slow codons near the start codon [13] (forming the equivalent of two closely-spaced defects near the start) suggests an expression-inhibiting, regulatory role for these initiation-end bottlenecks. Conversely, a finite number of well-separated defects at appropriate junctures provide pause points for local, successive protein folding with *minimal* reduction in current. Additional processes such as detachment, when combined with upstream or downstream bottlenecks can also regulate ribosome throughput.

The authors thank L. Shaw and A. B. Kolomeisky for valuable discussions. TC acknowledges support from the NSF (DMS-0206733), and the NIH (R01 AI41935).

References

- [1] Alberts, B. *et al.*, *Molecular Biology of the Cell*, (Garland Publishing, New York, 1994).
- [2] Bulmer, M. (1991) *Genetics*, **129**, 897-907.
- [3] Marais, G. & Duret, L. (2001) *J. Mol. Evol.*, **52**, 275-280.
- [4] Powell, J. R. & Moriyama, E. N. (1997) *Proc. Natl. Acad. Sci. USA*, **94**, 7784-7790.
- [5] Kurland, C. G. (1991) *FEBS Lett.*, **285**, 165-169.
- [6] Shimizu, Y., Inoue, A., Tomari, Y., Suzuki, T., Yokogawa, T., Nishikawa, K. & Ueda, T. (2001) *Nature Biotech.*, **19**, 751-755.
- [7] Spirin, A. S. (ed.), *Cell-Free Translation Systems*, (Springer-Verlag, New York, 2003).
- [8] Tsien, R. Y. (1998) *Annu. Rev. Biochem.*, **67**, 509-544.
- [9] Robinson, M., Lilley, R., Little, S., Emtage, J. S., Yarranton, G., Stephens, P., Millican, A., Eaton, M. & Humphreys, G. (1984) *Nucleic Acids Res.*, **12**, 6663-6671.
- [10] Sorensen, M. A., Kurland, C. G. & Pedersen, S. (1989) *J. Mol. Biol.*, **207**, 365-377.
- [11] Phoenix, D. A. & Korotkov, E. (1997) *FEMS Microbiol. Lett.*, **155**, 63-66.
- [12] Konigsberg, W. & Godson, G. N. (1983) *Proc. Natl. Acad. Sci. USA*, **50**, 687-691.
- [13] Chen, G. F. T. & Inouye, M. (1990) *Nucleic Acids*, **18**, 1465-1473.
- [14] Zhang, S., Goldman, E. & Zubay, G. (1994) *J. theor. Biol.*, **170**, 339-354.
- [15] Schütz, G. M. & Domany, E. (1993) *J. Stat. Phys.*, **72**, 277-296; Derrida, B., Domany, E. & Mukamel, D. (1992) *J. Stat. Phys.* **69**, 667-687; Derrida, B. (1998) *Physics Reports*, **301**, 65-83.
- [16] MacDonald, C. T. & Gibbs, J. H. (1969) *Biopolymers*, **7**, 707-725; Chou, T. (2003) *Biophys. J.*, **85**, 755-773; Shaw, L. B., Zia, R. K. P. & Lee, K. H. (2003) *Phys. Rev. E*, **68**, 021910.
- [17] Kolomeisky, A. B. (1998) *J. Phys A: Math. Gen.*, **31**, 1153-1164.
- [18] Arnoldi, W. E. (1951) *Quart. Appl. Math.*, **9**, 17-29; Saad, Y. *Numerical Solution of Large Eigenvalue Problems*, (Halsted Press, New York, 1992).
- [19] Bortz, A. B., Kalos, M. H. & Lebowitz, J. L. (1975) *J. of Comp. Phys.* **17** 10-18.
- [20] Lakatos, G. & Chou, T. (2003) *J. Phys. A: Math. Gen.*, **36**, 2027-2041.
- [21] Buschle, J., Maass, P. & Dieterich, W. (2000) *J. Stat. Phys.* **99**, 273-312.